J. Fluid Mech. (1997), *vol.* 350, *pp.* 1–27. Printed in the United Kingdom

© 1997 Cambridge University Press

Localized mixing due to a breaking internal wave ray at a sloping bed

By I. P. D. DE SILVA†, J. IMBERGER AND G. N. IVEY

Centre for Water Research, Department of Environmental Engineering,
The University of Western Australia, Nedlands, Western Australia 6907

(Received 18 March 1996 and in revised form 13 June 1997)

A laboratory experiment was conducted to investigate the characteristics of turbulence generated by an internal wave ray breaking on a sloping bed. The width of the incident wave ray was small compared to the bed length, so that an isolated turbulent patch was generated by the breaking process, a configuration unique to the present study. The parameter range covered subcritical, critical and supercritical frequencies. Flow visualization and velocity measurements revealed that near critical conditions the flow was confined to a narrow region above the bed and, contrary to expectations, critical waves showed a weak turbulence field. Subcritical and supercritical reflection resembled wave–wave interaction between the incident and the reflected waves and showed comparable centred displacement lengthscales. As the incident waves became progressively supercritical instabilities were first initiated away from the bed. For supercritical waves the centred displacement lengthscale and the turbulent Reynolds number both increased steadily up to about $\gamma \approx 2$, after which they started to decrease ($\gamma = \omega/\omega_c$, where ω is the frequency of the incident wave and $\omega_c = N \sin\beta$ is the critical frequency for an ambient uniform stratification of magnitude N and a bed angle of β). For subcritical waves an increase in the centred displacement lengthscale and the turbulent Reynolds number was also observed. The mixed fluid generated at the boundary collapsed into the fluid interior in the form of a horizontal two-dimensional viscous–buoyancy intrusion: the efficiency of mixing was, however, very small and no measurable change in the mean density gradient was observed over the duration of the experiments.

1. Introduction

With recent advances in field measurements the importance of boundary mixing as a means of nutrient circulation in the hypolimnion of lakes has become increasingly evident. Many observations have been reported supporting the existence of a turbulent benthic boundary layer in lakes (Wuest *et al.* 1994; Lemckert & Imberger 1995) and in oceans (Wunsch & Hendry 1972; Eriksen 1982, 1985; Wolanski 1987; Thorpe, Hall & White 1990; Toole, Polzin & Schmitt 1994; White 1994; Van Haren, Oakey & Garrett 1994; Ledwell & Hickey 1995). A number of plausible mechanisms can give rise to boundary mixing: bottom intrusions over topographically rough boundaries, turbidity currents, river inflows, basin-scale internal seiches, long internal Kelvin and Poincaré waves, and small-scale internal gravity waves are all possible driving mechanisms. Imberger (1995) identified some of these mechanisms from a field study

† Present address: Department of Mechanical Engineering, Sirindhorn International Institute of Technology, Thammasat University, PO Box 22, Thammasat-Rangsit Post Office, Pathumthani 12121, Thailand.

https://doi.org/10.1017/S0022112097006939 Published online by Cambridge University Press

of lake Biwa, Japan. It has been suggested (eg. Ivey & Nokes 1989; Garrett, MacCready & Rhines 1993) that breaking internal waves on slopes are the most likely driving mechanism for the benthic boundary layer, at least in the deep ocean.

In the present study we are only concerned with the turbulence and mixing characteristics generated by breaking internal gravity waves at a sloping bed. There is a wide variation in the bed slopes encountered in natural environments. In lakes bed slopes are in the range of 2°–20° (Wuest *et al.* 1994; Lemckert & Imberger 1995). In the ocean the r.m.s. slope of the sea bed is roughly 4°, but in the vicinity of seamounts slopes can be considerably higher in the range 6°–26° (Bell 1975). The benthic boundary layer acts as a buffer between the bulk lake interior and the very thin, nutrient rich, sediment interface (Baccini 1985). It is of immense importance for biologists and chemists to quantify the transport of matter through the benthic layer (for a review see Imberger 1994, 1995). In lakes and estuaries, boundary mixing due to breaking internal waves may provide a significant contribution to this transport, especially since it now appears (Imberger 1995) that the large-scale seiching motion due to Kelvin or Poincaré waves combines with groups of high-frequency nonlinear waves to give rise to small-scale medium-frequency modes; the frequencies of this ω^{-2} range of the spectrum correspond to the local critical frequencies for typical lake slopes.

In the context of internal wave breaking on sloping beds two types of configurations can be considered. Let us denote the dimensions of the benthic boundary layer by its height δ normal to the bed and the alongshore length by L. All the laboratory experiments (Cacchione & Wunsch 1974; Thorpe & Haines 1987; Ivey & Nokes 1989, 1990; Taylor 1993) carried out so far, except for the preliminary investigations by Ivey, De Silva & Imberger (1995) and De Silva, Imberger & Ivey (1995), were confined to breaking of a train of internal waves uniformly distributed over the sloping bed, so that $\delta/L \ll 1$; long, basin-scale shoaling internal waves also fall into this category. Most of the vertical transport of mass and momentum in this situation is maintained by complex shear dispersion flow (Imberger & Ivey 1993; Imberger 1994). The second category is where the internal waves are only incident on part of the bed. Mixing patches generated by these type of waves are localized with $\delta/L \sim O(1)$, and the communication of the benthic fluid with the lake interior is mainly due to localized horizontal intrusions. If the waves are forced for a time long compared to the wave period, ambient fluid from the top and bottom of the mixed patch is entrained to replenish the intruding benthic fluid, and an effective recycling of the benthic water is established. However, the internal waves generated in the stable thermocline in a lake beneath the surface mixing layer are made up of wave groups with a wide range of frequencies and wavelengths and of varying intensity, a description further complicated by intermittency in time and space. Such downward-propagating waves can also be created by the collapse of isolated mixed regions generated by local turbulent events (Wu 1969; McEwan 1973; Maxworthy & Monismith 1988; Teoh, Ivey & Imberger 1997). Accurate numerical modelling of the dynamics of lakes (Ogihara 1997) requires a detailed knowledge of the internal wave field in space and time. The mixing generated by such wave trains is better studied by taking into account the spatial and temporal variability of the waves and we have thus concentrated in this laboratory study on the case of localized rays of internal waves breaking on a sloping bed.

Reflection of internal gravity waves also plays an important role in the mid-ocean dynamics owing to the presence of ocean boundaries and abyssal hills which cover a sizeable area (Bell 1975) of the ocean floor. Low vertical diffusivities observed in the open ocean interior also suggest that most of the mixing should take place near such ocean boundaries (Garrett *et al.* 1993) in order to balance the overall vertical mass

https://doi.org/10.1017/S0022112097006939 Published online by Cambridge University Press

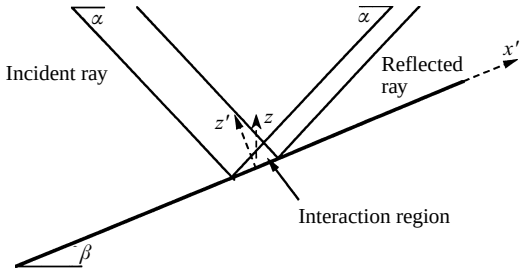


FIGURE 1. Schematic of the internal wave reflection from a sloping bed.

transport (Munk 1966). The suggestion of turbulence generated by mesoscale current drag aginst the sea floor (Armi 1978) was later shown to be implausible (Garrett 1979). With regard to lakes, Imberger (1994) showed that most of the energy supplied by the wind to the internal waves (basin-scale and small-scale) is not lost in the lake interior, but rather at the boundaries. Thus internal wave breaking at the boundaries seems to be the most viable candidate to account for the low but finite vertical diffusivities observed in the lakes (Imberger 1995; Etemad-Shahidi & Imberger 1997), and possibly in the ocean interior (Munk 1996).

Two-dimensional linear internal wave reflection on a sloping bed has been treated analytically by Phillips (1977). Eriksen (1985) extended the treatment to obliquely incident waves on a uniform slope and Thorpe (1987) considered the case of finite-amplitude waves. The boundary condition of zero normal velocity at the slope causes the reflected wave to retain the same frequency as the incident wave. However, an adjustment in the wavenumber and the amplitude of the reflected wave results. For the critical case, where the direction of the group velocity of the reflected wave coincides with the slope, the linear theory fails and the amplitude of the reflected wave increases without bounds. In the absence of rotation, the critical incident internal wave frequency is given by $\omega_c = N \sin\beta$ where β is the bottom slope from the horizontal and N is the background stable buoyancy frequency defined by $N^2 = (-g/\rho_r)\,\mathrm{d}\rho/\mathrm{d}z$ where g is the acceleration due to gravity, ρ is the fluid density, ρ_r is a reference density and z is the vertical coordinate.

It is convenient to define a parameter $\gamma = \omega/\omega_c$, so that $\gamma = 1$ indicates critically incident waves. Forward (supercritical) and backward (subcritical) reflecting waves are represented by $\gamma > 1$ and $\gamma < 1$, respectively. Figure 1 shows a schematic of linear reflection for the case $\gamma > 1$ where the wave interaction region is defined by the triangular region formed by the incident and reflected wave rays. Given the situation where both the incident and the reflected waves are stable individually, then instabilities should only occur in the interaction region. Thus it seems logical that, except for the case $\gamma = 1$ where the reflected wave is non-existent, the problem of wave reflection from the bed may be thought of as wave–wave interaction of incident and reflected wave rays, where the incident and reflected waves have the same frequency and phase but have different wavelengths and amplitudes.

Laboratory experiments reported by Teoh *et al.* (1997) and numerical studies by Javam, Imberger & Armfield (1997*a*) examined wave–wave interactions for waves of the same frequency and wavelength and showed that the resulting instabilities were generated by time-evolving nonlinear non-resonant interactions. Teoh *et al.* (1997) observed for their experimental configuration (with forcing frequency $\omega > N/2$) the existence of 2ω and higher harmonics which were clearly evanescent modes, and the same result was also observed in the numerical experiments of Javam, Imberger &

https://doi.org/10.1017/S0022112097006939 Published online by Cambridge University Press

Armfield (1997*b*) for all cases of $\gamma \neq 1$. Recent numerical work of Javam *et al.* (1997*b*), showed that for waves near $\gamma \approx 1$ the instabilities were triggered at the bed, while for $\gamma > 1$ such regions were triggered off the bed, an observation consistent with the present work. Their work also indicated that the reflection process for $\gamma > 1$ resembled the wave–wave interaction of incident and reflected waves above the bed (cf. Thorpe 1987) in that waves with superharmonic frequencies formed. For super-critical finite-amplitude waves, Thorpe (1987) showed that resonance between the incident and reflected waves can occur at higher order for chosen pairs of α and β, where α is the inclination of the incident wave group velocity to the horizontal. At second order this can occur for small bed angles, specifically $\beta < 9°$.

The thickness δ of the boundary layer is determined by the properties of the incident wave field for given ambient conditions. According to Ivey & Nokes (1989), for the bottom boundary layer to form the Reynolds number defined by, $\omega\zeta^2/\nu$, where ζ is the wave amplitude and ν the kinematic viscosity, has to be greater than 15–20. The resulting boundary layer thickness was found to be $\delta \approx 5\zeta$. From re-examination of their data and that of Taylor (1993), Ivey *et al.* (1995) suggested that in fact $\delta \approx 0.15\lambda_v$, where λ_v is the wavelength of the incident waves measured normal to the bed, a result which also appears to be consistent with available field data but smaller than the observations from the numerical work of Slinn & Riley (1996) who found $\delta \approx 0.25\lambda_v$. According to previous laboratory experiments δ varies spatially over the alongshore length and temporally over a wave cycle, but near $\gamma \approx 1$ this variability was lower. For critically incident internal waves on a 20° bed, Taylor (1993) argued that the boundary layer flow consisted of two phases: a relatively calm downslope flow and a more energetic upslope flow and this was the main source of the temporal variability.

In regard to the energetics of the wave breaking, a fraction of the energy of the incident wave is radiated away as the reflected ray and a part of the energy is lost due to turbulent dissipation. The rest is converted into irreversible mixing which accounts for the vertical transport of mass and matter. Experiments by Ivey & Nokes (1990) for critically incident waves on 30° bed showed the mixing efficiency, defined as the ratio of the increase in potential energy to the loss of kinetic energy by the incident waves, had an upper bound of approximately 0.20; the mixing efficiency reaching a maximum at $\gamma \approx 1.2$. For highly subcritical ($\gamma < 1$) waves nearly zero mixing efficiency and hence buoyancy flux were observed. Recent numerical work by Slinn & Riley (1996) suggested a slightly higher mixing efficiency of about 0.35 for critically reflected internal gravity waves independent of the slope angle. According to their analysis, 35% of the incident energy was utilized in mixing the stratified fluid, 55% was dissipated into heat and approximately 10% of the energy was re-radiated away from the turbulent boundary layer.

The present work was motivated by the fact that collapsing turbulent patches often generate internal wave ray tubes that are incident only on part of the lake boundary. Numerical schemes which use internal wave ray tracing techniques also require knowledge of reflection process at boundaries for each ray tube. The configuration of the present experiments was chosen to investigate such situations.

2. Experiments

The experiments were conducted in a glass-walled tank of dimensions 590 cm × 54 cm × 60 cm. The internal wave rays were generated using a multi-bladed folding paddle, adapted from the pioneering work of McEwan (1973), made up of eight 5 cm × 53.5 cm hinged blades each covering the entire width of the tank (see figure 2

https://doi.org/10.1017/S0022112097006939 Published online by Cambridge University Press

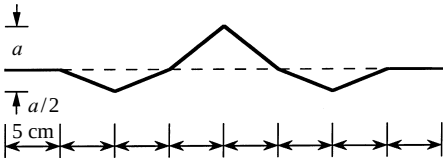


FIGURE 2. Schematic of the wave paddle.

and Teoh *et al*. 1997). The wave ray tube generated by the paddle was approximately 1.5 wavelengths wide while the horizontal wavelength of the wave was 20 cm. The amplitude of the outermost portions of the paddle was half that of the middle portion, so that no net volume displacement of the fluid occurred, thus eliminating unwanted fluid circulation within the tank. The work of McEwan (1973) indicated that the waves generated by such paddles have a dominant first mode. However, a series of different experiments were conducted with the same amplitudes on all portions of the paddle to promote mixing. The former set of experiments is identified, where appropriate, with the symbol * next to the paddle amplitude a in the discussion below. In each experiment the paddle was submerged at least 2 cm below the surface to reduce the generation of surface waves. Approximately 2 cm thick sponge strips were placed on the two outermost edges of the paddle to prevent any disturbance to the ambient fluid, which was otherwise quiescent. The side clearance between the end of the paddle and the tank walls was about 0.3 cm. The paddle was mechanically linked to an eccentric wheel and driven by a heavy-duty adjustable-speed stepper motor. By varying the eccentricity of the wheel, the paddle amplitude could be varied. In this study, 2.0, 2.45, 2.9 and 3.1 cm paddle amplitudes were used. The lengths of the slender-linkage rods connecting the paddle blades and the eccentric wheel were large compared to the eccentricity (typically in the range of 50 : 1), so that the motion of the paddle was very nearly sinusoidal.

A 2 cm thick Plexiglas plate, which served as the sloping bed, was installed in one end of the tank. The plate was pivoted at 12 cm from the tank bottom, so that the bed angle could be varied while keeping the pivotal axis fixed. The range of the bed angles covered in the experiment was 5° to 45°. The pivotal axis, around which all the measurement and flow visualization were done, also corresponded to the centre of the incident wave ray.

The tank was filled with a linearly stratified salt solution using the standard two bucket technique. The depth of the water column was 48 cm. Before starting each experiment the tank was left for about 24 h in a temperature-controlled room to achieve an equilibrium stable temperature. The temperature of the fluid medium was measured using a FP07 fast response thermistor, while the salinity was simultaneously measured using both a siphoning and a four-electrode microscale fast-response conductivity probe. Since the drift in the suction conductivity probe was less than 0.2% over 10 h, the four-electrode fast-response conductivity probe was calibrated *in situ* against the siphoning conductivity probe. The spacing between the tips of the three probes was about 0.4 cm. The probe assembly was mounted on a computer-controlled stepper-motor-driven linear bearing whose traversing speed was accurately monitored by a slew signal. The direct and differentiated output from each sensor was recorded at 100 Hz through a 16-bit analog-digital converter. A traversing speed of 10 cm s^{-1} was used; thus the Nyquist wavenumber cut off was 500 cycles m^{-1}. Prior to the experiments, the thermistor was calibrated using an accurate platinum resistor thermometer and the conductivity probes were calibrated using saline samples whose densities were accurately measured using an Anton–Parr digital densitometer. In all

https://doi.org/10.1017/S0022112097006939 Published online by Cambridge University Press

cases third-order polynomials were used as the calibration curves. Three different flow visualization methods were employed. A rainbow colour schlieren system, as described in Ivey & Nokes (1989), was used to obtain flow images and also to ensure that the sampling probes pass through the intended flow regime. This was sometimes complemented by shadowgraph images. The overall flow pattern and the formation of intrusions were visualized using dye samples as passive tracers.

The velocity field of the interaction region was quantified using a digital particle tracking method (Maximum Cross-Correlation) as described in Stevens & Coates (1994). The MCC technique essentially consisted of maximizing the cross-correlation between two video frames of particle images separated by a known time interval. The particles, containing pigments of rhodamine and sodium fluorescein dye, were injected slowly into the flow field before the beginning of the experiment. An argon-ion (4 W) vertical laser sheet of approximately 5 mm thickness was used to illuminate the particles across the mid-section of the tank. The resulting flow patterns were recorded on super-VHS format for subsequent analysis. The video images were digitized using an ITEX frame grabber with 10-bit range in intensity. The images contained intensity information of (768×568) pixels, so that depending on the physical area imaged the spatial resolution could be estimated.

3. Results

3.1. *Schlieren visualization*

The details of the Rainbow colour schlieren system are adequately described by Howes (1984, 1985), Ivey & Nokes (1989) and Taylor (1993). Figure 3(*a*, *b*) shows schlieren images of the interaction region of the incident wave and the reflected wave at slightly supercritical and highly supercritical conditions, respectively. The vertical lines in the images are 10 cm apart. The point of intersection of the vertical centreline of the two vertical bars with the slope corresponds to the centre of the incoming wave ray tube. These images are different from those of Ivey & Nokes (1989) due to the fact that in the present experiment the incident ray tube was local, whereas in Ivey & Nokes (1989), the wave forcing was present over the entire slope. The rainbow filter of diameter 2.54 cm used in the schlieren system consisted of annular colour rings of blue at the centre, yellow, green, red and black at the outermost ring. The colours depicted in the images are an indication of the amount of the light deflected by the fluid medium which in turn was proportional to the gradient of the refractive index. For aqueous solutions of low concentrations of NaCl, the refractive index (μ) is linearly related to its density by $\mathrm{d}\mu/\mathrm{d}\rho = 0.2431\ \mathrm{gm^{-1}\,cm^3}$. Thus, the colours can also be used to estimate the instantaneous density gradient of the fluid. The deflection (η) at the exit plane of a normally incident beam of light is given by (Howes 1984),

$$\eta = \frac{1}{2}\frac{\mathrm{d}\mu}{\mathrm{d}\rho}\frac{\mathrm{d}\rho}{\mathrm{d}z}W^2, \tag{1}$$

where W is the width of the tank. In the present experimental set up the maximum η, which corresponds to colour black, observable is 1.27 cm, $W = 54$ cm, and the focal length of the converging mirrors is 244 cm, hence the black regions in figure 3 indicated a density gradient of $\mathrm{d}\rho/\mathrm{d}z \approx 7.9 \times 10^{-4}\ \mathrm{gm\,cm^{-4}}$. For a density stratification of $N = 0.921\ \mathrm{rad\,s^{-1}}$ ($\mathrm{d}\rho/\mathrm{d}z \approx 8.6 \times 10^{-4}\ \mathrm{gm\,cm^{-4}}$), this implied that the black regions, which were the regions of weakest density gradients, could be statically unstable.

About two wave periods after the initiation of the paddle forcing colour bands depicting the different density gradients were visible above the bed. The angle of

https://doi.org/10.1017/S0022112097006939 Published online by Cambridge University Press

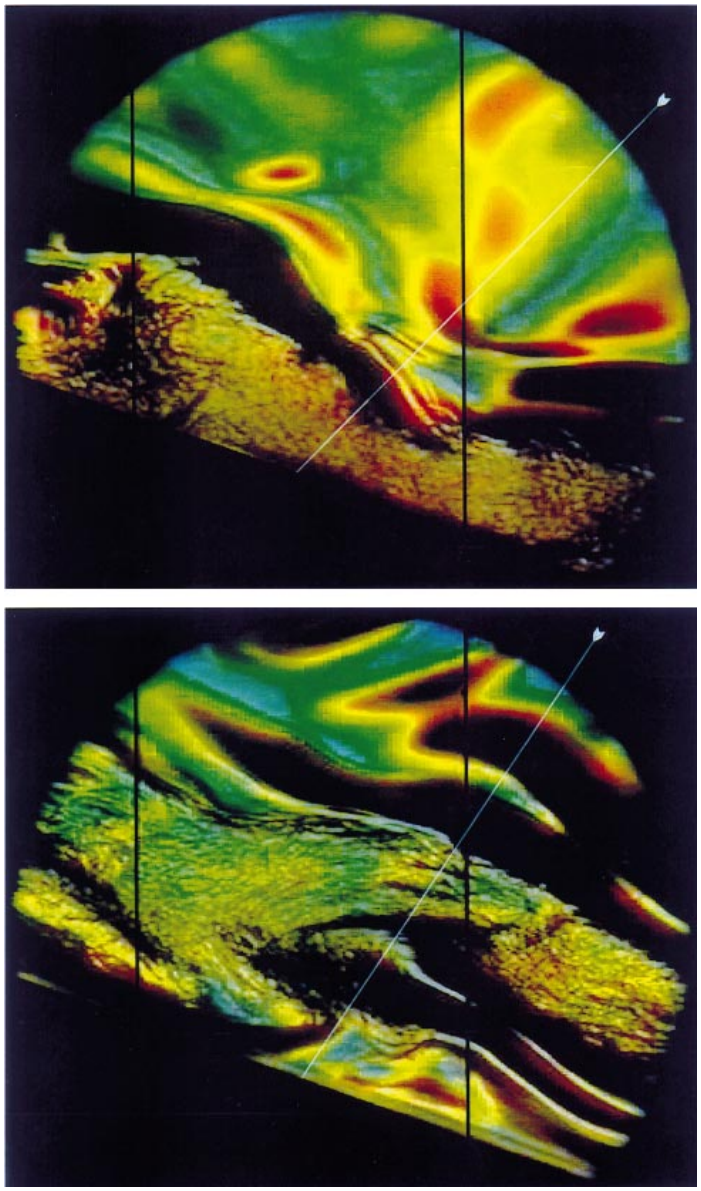


FIGURE 3. Schlieren video images showing the on-slope and off-slope initiation of instabilities depending on γ. The experimental conditions are $a^* = 2$ cm, $N = 0.921$ rad s^{-1}, $\beta = 20°$. (*a*) $\alpha = 45°$, $\gamma = 2.07$; (*b*) $\alpha = 56°$, $\gamma = 2.43$. The vertical lines in each figure are 10 cm apart. The oblique thin white line indicates the centreline of the incident wave ray.

inclination of the bands to the vertical was in agreement with the linear ray theory. As the waves approached the bed, the density gradients were alternately weakened and sharpened in the region above the bed. This was clearly visible on the images as black coloured banded regions near the bed, while away from the slope the colour remained near green or yellow indicating moderate changes in the density gradient. In all experiments, instabilities first occurred in the black regions and once the instabilities were initiated, the interaction region soon became turbulent as indicated by the 'mingling' of colours.

https://doi.org/10.1017/S0022112097006939 Published online by Cambridge University Press

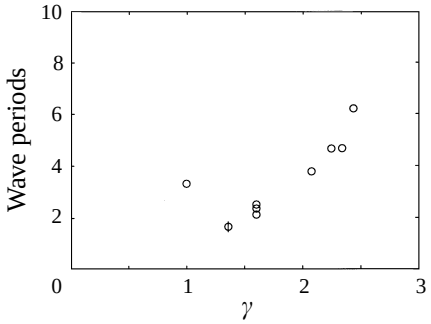


FIGURE 4. The variation of time (in wave periods) at which the instabilities were first observed in the schlieren images. Time $t = 0$ is taken as the time taken by the waves to arrive at the bed from the paddle. The experimental conditions are: $a^* = 2.0$ cm, $N = 0.921$ rad s^{-1}. The vertical line centred in one of the symbols indicates the errorbar.

For incident waves closer to the critical condition, or moderately supercritical, the instability region was initially triggered near the bed (figure 3*a*). An interesting observation made in the series of experiment was that as the incident wave became progressively more supercritical, the initial instabilities began to form away from the bed (figure 3*b*). However, after a few more wave cycles the size of this region of instabilities gradually developed and extended down to the bed. According to Thorpe (1987), nonlinear effects reduce the steepness of the incoming waves and promote low statically stable regions away from the slope, for supercritical waves. Consistent with previous experiments, the turbulent boundary layer did not form until a few wave cycles after the commencement of paddle forcing. Figure 4 depicts the time (in wave periods) at which instabilities were first observed in the schlieren images after the arrival of the first train of waves at the bed.

3.2. *Vertical density profiles*

Vertical casts or density profiles were used to quantify the turbulence generated by the breaking events. The process involved two stages. First, the recorded profiles with overturns were monotonized to obtain the statically stable state which was associated with the minimum potential energy. The vertical distances l_d each fluid parcel had to be displaced to achieve the monotonized profile are known as the Thorpe displacements (Thorpe 1977). Using the values of l_d, an appropriate lengthscale l_c of the energy-containing eddies was calculated as outlined in Imberger & Boashash (1986). The centralized lengthscale l_c is calculated by moving the displacement scales l_d by one-half of the l_d values themselves to the centre of the event. For an ideal overturning event having complete solid-body rotation of the fluid, this procedure removes the events having maximum displacements at the boundaries of the patch (see Imberger & Boashash 1986). This centralized lengthscale l_c was used in estimating the appropriate non-dimensional numbers which will be discussed later in §3.6.

In figures 5 and 6, we present a series of vertical casts of density profiles taken through the vertical centreline of the interaction region, the displacement scales and the resulting buoyancy anomalies for two different experiments with $\alpha = 45°$, $\gamma = 2.06$ and $\alpha = 26.7°$, $\gamma = 1.31$, respectively. In both figures the time interval between two consecutive profiles was 1/7 of the corresponding wave period. The magnitudes of l_d and g' show a definite variation through the wave cycle. Note that the buoyancy anomalies observed in figure 5(*c*) (compare profiles 2 and 3), are not proportional to the displacement scales shown in figure 5(*b*), even though the initial density

https://doi.org/10.1017/S0022112097006939 Published online by Cambridge University Press

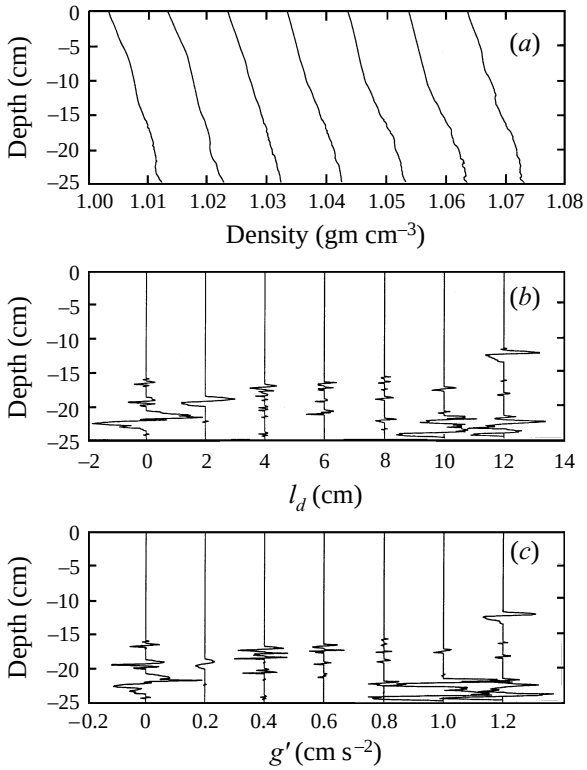


FIGURE 5. (*a*) The Density profiles taken through the vertical centreline of the interaction region for seventh wave cycle. The time interval between the profiles is $T/7$, where T is the incident wave period. Except for the leftmost profile, each other profile is offset by 0.01 gm cm^{-3}. (*b*) The displacement scale l_d, for the profiles shown in (*a*). Except for the leftmost profile, each other profile is offset by 2 cm. (*c*) The buoyancy anomaly g', for the profiles shown in (*a*). Except for the leftmost profile, each other profile is offset by 0.2 cm s^{-2}. The experimental conditions are $a = 2.9$ cm, $N = 0.641$ rad s^{-1}, $\alpha = 45°$, $\beta = 20°$.

stratification was linear. This was caused by the changes in the initial linear stratification by the straining of the density field due to the waves and mixing. This disparity may be explained as follows: consider a discretely sampled density profile $\rho(i)$, $i = 1$ to m, at intervals of Δz in the vertical: The buoyancy anomaly at the ith point is defined by $g'(i) = g[\rho(i) - \rho_0(i)]/\rho_r$ where $\rho(i)$ and $\rho_0(i)$ are the instantaneous and the monotonized density distributions. Let $\rho_0(j)$ be the density in the monotonized profile corresponding to density $\rho(i)$ (so that the jth point in the ρ_0 profile and the ith point in the ρ profile have the same density), then

$$g'(i) = \frac{g}{\rho_r}[\rho_0(j) - \rho_0(i)] = \Delta z \sum_{i}^{j} M^2(k), \quad i \neq j, \tag{2}$$

where $M^2(k)$ is the vertical density gradient of the monotonized density profile $\rho_0(z)$. Note that if the instantaneous profile $\rho(z)$ does not contain any overturns then such pairs of i and j do not exist, and consequently (2) is not valid.

This procedure excludes pure wave-like motions which do not contain any overturns. Note that the displacement scale $l_d = \Delta z(j - i)$. For constant Δz, the buoyancy anomaly is strictly dependent on the local monotonized buoyancy frequency between the points i and j, according to (2). The sorted profile $\rho_0(i)$ can be different

https://doi.org/10.1017/S0022112097006939 Published online by Cambridge University Press

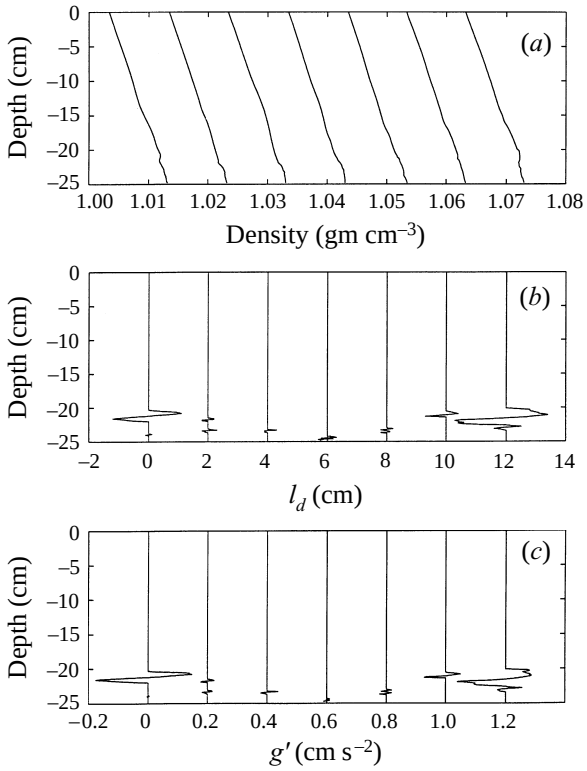


FIGURE 6. Same as figure 5, but for $\alpha = 26.7°$.

from the initial density distribution only through turbulent and molecular diffusion and by the straining of the isopycnals by the wave motion. Thus the buoyancy anomaly observed in a turbulent stratified environment is due to a combination of the actual displacement of fluid parcels and the straining of the density field. In light of the present experiments, we may estimate the contribution due to the straining of the density field. The contribution to $M^2(k)$ from a linear internal wave field is purely sinusoidal and its amplitude can be shown to be (Phillips 1977), $N_0^2\,an$, where N_0 is the initial buoyancy frequency, a is the wave amplitude and n is the vertical wavelength. The parameter an is usually termed the wave steepness. Thus the buoyancy anomaly is changed by a factor of an due to the presence of the wave field. The relatively large buoyancy anomalies observed at different phases of the wave were indicative of the nonlinearity of the resulting density distribution.

3.3. *Spatial extent of the boundary layer*

The height normal to the bed of the wave interaction region (the triangular region formed by the incident wave, the reflected wave and the bed shown schematically in figure 1) is given by the geometry as

$$h = \lambda \frac{\sin|\alpha - \beta|}{2\cos\alpha} \tag{3}$$

for both subcritical ($\alpha < \beta; \gamma < 1$) and supercritical ($\alpha > \beta; \gamma > 1$) cases. Here λ is the horizontal wavelength, α is the inclination of the group velocity vector of the incident wave to the horizontal, and β is the inclination of the bed to the horizontal. The magnitude of h depends on the absolute value of $\alpha - \beta$. Thus, for a given incident

https://doi.org/10.1017/S0022112097006939 Published online by Cambridge University Press

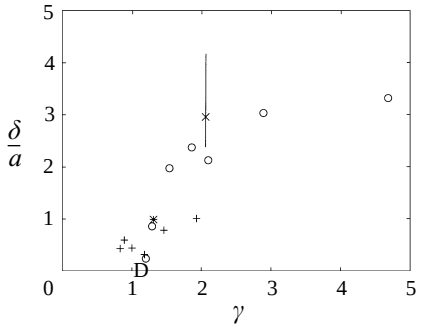


FIGURE 7. The variation of non-dimensional cycle-averaged boundary layer thickness with the parameter γ: ○, $a = 3.1$ cm, $N = 0.615$ rad s^{-1}, $\omega = 0.485$ rad s^{-1}; +, $a = 3.1$ cm; $N = 0.615$ rad s^{-1}, $\omega = 0.298$ rad s^{-1}; ×, $a = 2.9$ cm; $N = 0.641$ rad s^{-1}, $\omega = 0.453$ rad s^{-1}; ∗, $a = 2.9$ cm; $N = 0.641$ rad s^{-1}, $\omega = 0.288$ rad s^{-1}; D, $a = 3.1$ cm; $N = 0.588$ rad s^{-1}, $\omega = 0.365$ rad s^{-1}.

wave field (constant α) changing the slope angle β above and below the critical angle ($\beta = \alpha$) by the same amount results in the same h.

The thickness δ of the benthic boundary layer may be defined as the distance above the bed beyond which the displacement scale l_d vanishes. From figures 5 and 6, a strong temporal variation in the thickness of the boundary layer is evident in both cases. However, comparison of the two figures should be done with caution: while both experiments were conducted with the same bed slope of 20°, for the run shown in figure 5 with higher γ (hence higher ω), there was more incident wave energy being imparted into the boundary layer per unit time than for the run shown in figure 6. As a result the boundary layer region appears to be more turbulent in figure 5.

In quantifying the boundary layer thickness, for each run several vertical profiles through the centreline of the interaction region were taken. The thickness δ was calculated as the statistical mean of the distances from the bed to the point at which l_d became zero; see figures 5 and 6, for example. Although this method yielded a temporally averaged value it excluded the spatial variability. A simple energy argument was then used to obtain a vertical scale for the turbulence caused by wave breaking. For a given wave amplitude a the maximum amount of energy available per unit mass is of order a^2N^2 and for a background stratification N one complete overturn will have a scale a. In this simplified treatment, all the incident wave energy was assumed to be expended in realizing one overturn and the production of a buoyancy flux, while local energy dissipation and energy carried away by the reflected waves are neglected, effects which will be considered later, in §3.7. In figure 7, the variation of non-dimensional boundary layer thickness δ/a with γ is shown. The boundary layer thickness δ was taken as the average of the distances from the point at which $l_d = 0$ to the bed over different phases in one wave cycle. The errorbar shown indicates the maximum and minimum values observed for that particular data point.

In reality, the amount of energy available to create an overturn is less than a^2N^2, hence δ/a should be less than unity. However, as the size of the interaction region increases with increasing γ, the overturn regions are rather patchy and segmented and there is more than one overturn (for example, see the displacement scales l_d in figures 5 and 6 which show there are stable regions sandwiched between the unstable regions). Since δ is defined as the total extent over which these unstable signatures were observed, δ/a can be greater than unity, as seen in figure 7 for the supercritical runs. The figure also shows a definite decrease in thickness of the boundary layer as the incident waves become close to critical. Although the parameter range is limited for

https://doi.org/10.1017/S0022112097006939 Published online by Cambridge University Press

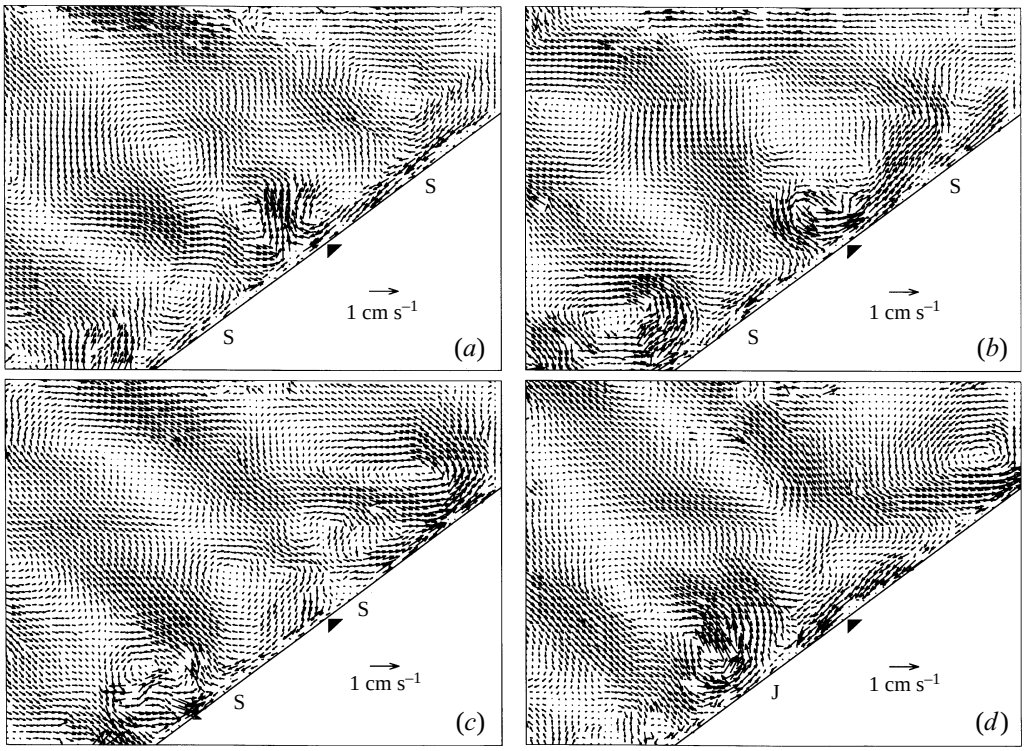


FIGURE 8. A sequence of velocity field images of the seventh wave cycle for a critically incident wave field at the interaction region. The experimental conditions are: $a = 3.1$ cm, $N = 0.588$ rad s^{-1}, $\omega = 0.365$ rad s^{-1}, $\gamma = 1.00$. The time interval between the images is approximately $T/4$: (*a*) $t = 120$ s, (*b*) 124 s, (*c*) 128 s, (*d*) 132 s. The imaged area shown in each panel is 23.4 cm × 18.5 cm. The solid triangle in each panel at the slope indicates the centre of the interaction region.

subcritical cases, a steady increasing trend in the non-dimensional boundary layer thickness is evident. The increase in lengthscales can also be seen later in figure 13. This result is different from the relation $\delta \approx 0.12\lambda_v$ reported by Ivey *et al.* (1995). The disparity may be due to the following: (i) the relation given by Ivey *et al.* (1995), as was also suggested by Slinn & Riley (1996), was valid strictly only for critically incident waves; (ii) the boundary layer thickness for supercritical runs shown in Ivey *et al.* (1995) (their figure 5) was based on schlieren observations (although they found a few supporting data points from density microstructure profiles of Taylor (1993) for critically incident waves), whereas the present data were all extracted from the vertical profiles of density; (iii) the data of Ivey *et al.* (1995) were both spatially and temporally averaged as opposed to the present data which were only temporally averaged.

3.4. *Velocity field in the interaction region*

Figure 8 shows a series of velocity images of the interaction region, corresponding to the seventh cycle, for a critically incident wave field with $a = 3.1$ cm, $\alpha = \beta = 38.4°$ and $\gamma = 1$. The time interval between two consecutive images was approximately $0.25T$, where T is the wave period. The solid triangle on each of the images indicates the position where the centreline of the incident ray beam intersected the bed, where the incident wave ray spanned diagonally across each figure. The wave field described here essentially contained only the incident wave ray as the effect of the reflected wave was minimal.

https://doi.org/10.1017/S0022112097006939 Published online by Cambridge University Press

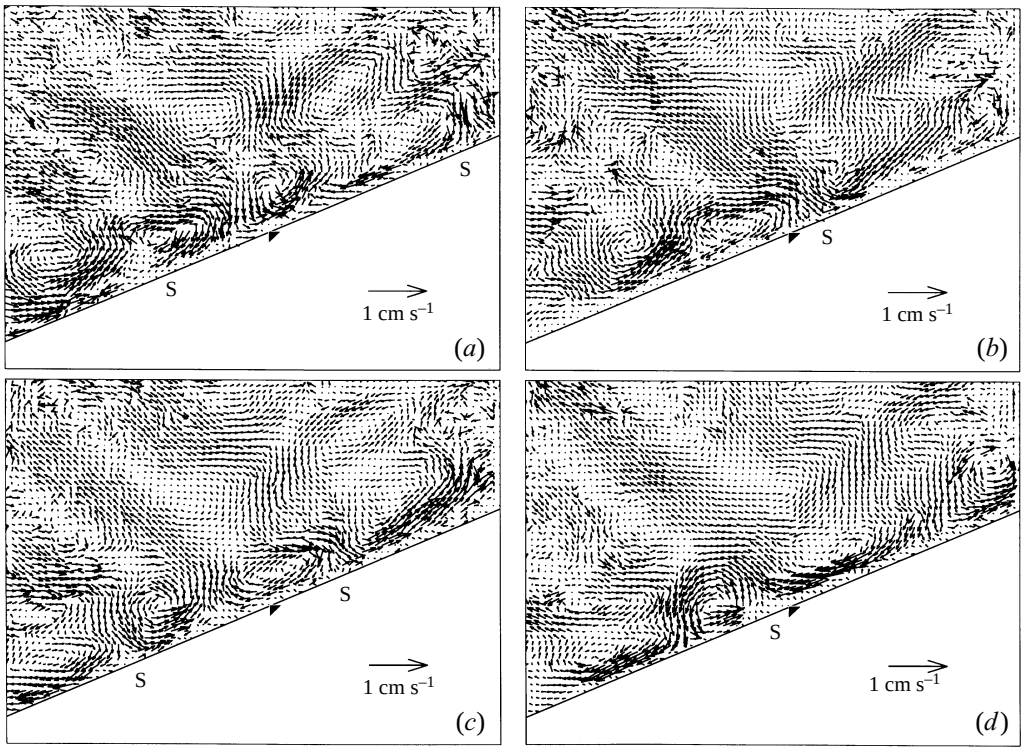


FIGURE 9. A sequence of velocity field images near the interaction region for a supercritically incident wave field. The ninth wave cycle is shown. Experimental conditions are: $a^* = 2.0$ cm, $N = 0.588$ rad s^{-1}, $\beta = 23.3°$, $\omega = 0.365$ rad s^{-1}, $\gamma = 1.57$. The wave period is 17.2 s. The imaged area shown in each panel is 30.4 cm $\times$ 23.7 cm. (*a*) $t = 156$ s, (*b*) 160 s, (*c*) 164 s, (*d*) 168 s.

Far from the sloping bed, in all panels, the velocity structure of the oblique incoming wave can be seen. Near the bed, this wave field was distorted by a persistent and dominant alongslope flow resembling a turbulent bore. Near vertical motion above the middle of the bed (figure 8*a*, *b*) and an eddy-like structure at mid-slope were due to the interaction of the incident wave and the alongslope flow which caused the fluid motion to separate from the bed. In the next quarter of the cycle (figure 8*c*), the incident wave field reversed direction, as did the swirling eddies and the alongslope flow. The stagnation points in the flow field in all panels are marked S. Subsequently, strong downslope and upslope flows caused an ejection of fluid away from the bed and a jet-like structure is shown in the last quarter of the cycle (figure 8*d*, marked J). From the schlieren images, the motion inside the jet seemed to be turbulent throughout the cycle. This sequence of events was repeated in each wave cycle and the net result was an almost horizontal periodic intrusion into the main fluid body. The motion above the bed showed a strong spatial inhomogenity and except for the moving turbulent bore, the rest of the motion seemed to be relatively calm. Apart from the collision of upslope and downslope flows which caused the fluid injection, most of the motion, other than the incident wave motion, was confined to a narrow region above the bed. With the no-slip boundary condition at the bed this implied that most of the incident energy had to be dissipated in this narrow region near the bed and as we will see in §3.6 below, the magnitudes of the cycle-averaged overturn lengthscales were small.

In figure 9 we show the velocity images for an incident wave field as in figure 8, but at a different slope angle of $\beta = 23.3°$ ($\gamma = 1.57$) and with a lower paddle amplitude

https://doi.org/10.1017/S0022112097006939 Published online by Cambridge University Press

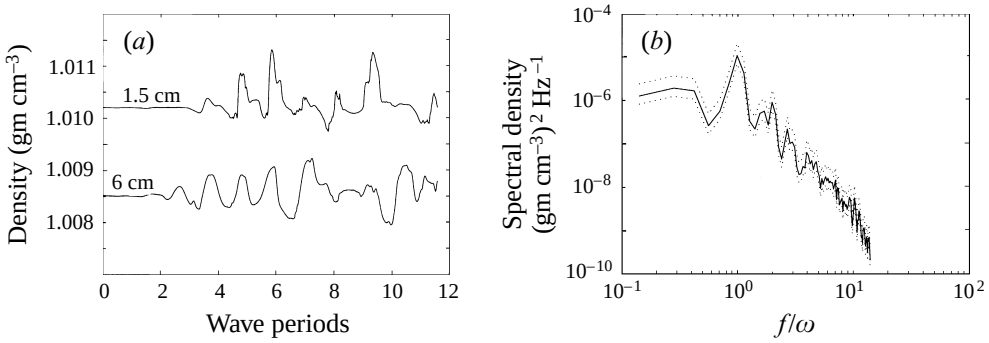


FIGURE 10. (*a*) Time series records of density at two points ($z = 1.5$ cm and 6.0 cm) in the vertical centreline of the interaction region. $N = 0.615$ rad s^{-1}, $\omega = 0.432$ rad s^{-1}, $a = 3.1$ cm, $\gamma = 1.32$. Time $t = 0$ is taken as the initiation of paddle forcing. (*b*) The spectrum of the density fluctuations recorded 1 cm above the bed in the centre of the interaction region. $a^* = 2.0$ cm, $N = 0.922$ rad s^{-1}, $\alpha = 33.2°$, $\beta = 20°$, $\gamma = 1.60$. The dotted lines indicate the 95% confidence limits.

$a = 2.0$ cm in order to illustrate how the velocity field was influenced by the presence of a reflected wave ray. Note the reduction in the magnitudes of the velocity due to the decrease in paddle amplitude. The particular images shown correspond to the 9th wave period since the beginning of the paddle motion. In all figures towards the mid-left and mid-right of the panel the incident wave and reflected wave rays can be seen, although they are somewhat distorted by the motion remaining from the previous cycle. One major difference here from that observed in the critical run is that the flow parallel to the bed took place slightly above the bed. The magnitude of the velocity vectors very near to the bed have decreased compared to that of the critical case (figure 8). The eddy motion also extended further off the bed than in the critical case, a result of the increase in the extent of the wave interaction region, as given by (3). This area where increased eddy motions were present were also clearly seen in the schlieren observation. The velocity field appeared more complex, showing more recirculating eddies with some irregular flow patterns, and the regular internal wave motion was difficult to resolve. The increase in the extent of the wave interaction region allowed a larger region for overturning to take place, compared to the critical case presented in figure 8. As a result, the magnitude of the overturning lengthscales increased (see §3.6).

3.5. *Time series of density records*

Figure 10(*a*) shows the time series of the density records for a run with $\gamma = 1.32$ at two different elevations: $z = 1.5$ cm and $z = 6.0$ cm along the vertical centreline of the interaction region. Note that for the given experimental parameters $z = 1.5$ cm lies within the interaction region whereas $z = 6$ cm lies outside it. At both locations a continuous increase in magnitude of the density variations with time can be seen up to approximately six wave periods at which point the wave amplitudes continued to grow until such time that they were large enough to cause instabilities and prevent further growth. Of the two isopycnal displacement records, note that the one closer to the bed ($z = 1.5$ cm) underwent the breaking earlier. This is consistent with the observation shown in figure 3 that for moderately supercritical waves the instabilities first developed near the bed. The power spectral density of the density fluctuations shown in figure 10(*b*) exhibited a weak peak at the frequency 2ω. For this particular run $2\omega > N$, so this is an evanescent wave mode which should decay rapidly with the vertical distance from the disturbance source. Numerical simulation on wave–wave

https://doi.org/10.1017/S0022112097006939 Published online by Cambridge University Press

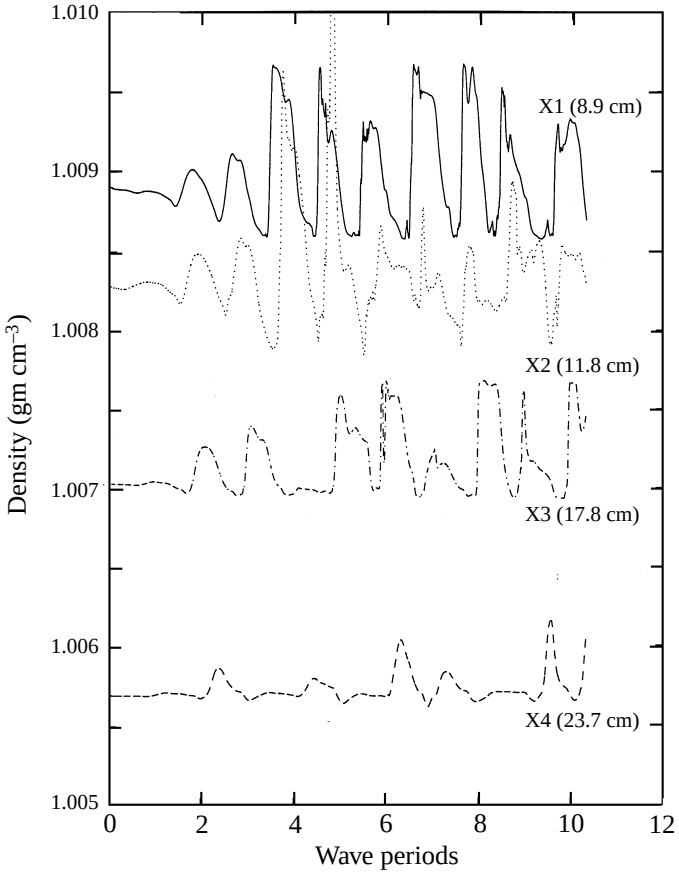


FIGURE 11. Time series records at the locations X1, … , X4, showing the existence of an upslope flow parallel to the bed. The locations are defined by (x', z') coordinates in cm (8.9, 0.8), (11.8, 0.8), (17.8, 0.8) and (23.7, 0.8), respectively. The experimental conditions are as given in the caption of figure 10(*a*).

interactions and reflection of internal waves at boundaries by Javam *et al.* (1997*a*, *b*) and the laboratory experiments of Teoh *et al.* (1997) on wave–wave interactions also showed similar features.

To investigate the alongslope flow which dominated near the critical conditions, time series of density records were obtained in one experiment at four upslope locations (figure 11). When the upward-moving bore carrying higher-density deeper fluid reached the conductivity probe, a sudden rise in the density was observed (station X2, between periods 4 and 5). The bore, which resembled the head of an upward-moving gravity current, had a rotational motion and that enhanced the density gradient between the bore and the ambient fluid. At later stages, when it reached stations X3 and X4, the spinning motion of the head had diminished and the density jump had weakened. Near the centre of the interaction region, the density fluctuations had a regular oscillating behaviour as is clearly seen for the data at X1, whereas far from the centre at stations X3 and X4, for example, this feature was not as clear. This was probably due to the motion remaining from the previous cycles and also due to the increased relative influence of the background wave motion. It should be mentioned that all locations from X1 to X4 were upslope from the centre of the interaction region

https://doi.org/10.1017/S0022112097006939 Published online by Cambridge University Press

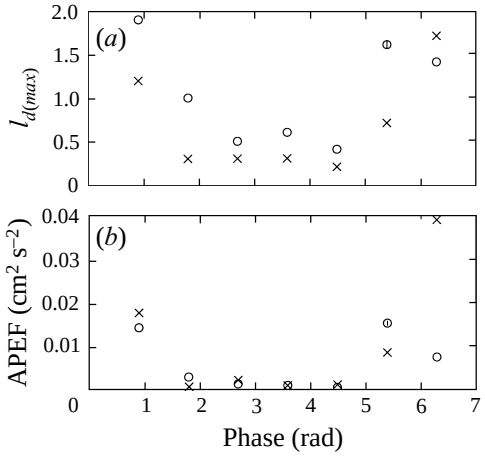


FIGURE 12. (*a*) The variation of maximum displacement scales over a wave cycle. (*b*) The variation of available potential energy of the fluctuations (APEF) over a wave cycle; ×, for the run given in figure 5; ○, for the run given in figure 6.

and no density records at downslope locations were recorded. However, flow visualization using the shadowgraph technique revealed the existence of a complementary downslope flow.

3.6. *Turbulent quantities*

Based on the turbulent lengthscale l_c (see §3.2) non-dimensional numbers associated with stratified turbulence may be defined as (Ivey & Imberger 1991; Imberger 1994): the turbulent Reynolds number $Re_t = ul_c/\nu$; the turbulent Froude number $Fr_t = u/Nl_c$; and the small-scale turbulent Froude number $Fr_\gamma = (\epsilon/\nu N^2)^{1/2}$, where ϵ is the rate of kinetic energy dissipation, $u = (\epsilon l_c)^{1/3}$ is the r.m.s. velocity fluctuations if l_c is representative of the scale of energy-containing eddies, and ν is the kinematic viscosity. The instantaneous kinetic energy dissipation rate ϵ was obtained by curve fitting a theoretical Batchelor spectrum for the temperature gradient (Batchelor 1959) to the measured temperature gradient spectra (Dillon & Caldwell 1980; Imberger & Boashash 1986; Luketina 1987; Teoh *et al*. 1997; Grigg & Ivey 1997) taking ϵ as a free parameter. Based on the resolution of the sensors used in the study, dissipation rates in the range of 10^{-10}–10^{-5} m^2 s^{-3} could be successfully resolved (Luketina & Imberger 1989; Teoh *et al*. 1997; Grigg & Ivey 1997). A typical record length was 12.8 cm where the portion of the wavenumber spectra from the maximum to the roll-off region was used for curve fitting.

Re_t can be interpreted in terms of energy as either the ratio of the rate of actual energy being dissipated to the rate of dissipation by viscous action on motions of scale l_c or in terms of timescales as the ratio of the time it takes for momentum to be diffused by viscous action to the time it takes for the turbulence to advect the fluid element by l_c (Imberger 1994). In the same way, Fr_t can be interpreted as either the ratio of the rate of dissipation to the rate of release of potential energy or as the ratio of the time it takes for an unstable fluid parcel to return to its neutral position to the time it takes to mix the buoyancy anomaly. The small-scale Froude number Fr_γ is often used as a parameter which indicates the existence of a buoyancy flux. The grid-generated turbulence experiments of Stillinger, Helland & Van Atta (1983) and Itsweire, Helland & Van Atta (1986), for example, indicated that when $Fr_\gamma > 4$ a buoyancy flux exists.

https://doi.org/10.1017/S0022112097006939 Published online by Cambridge University Press

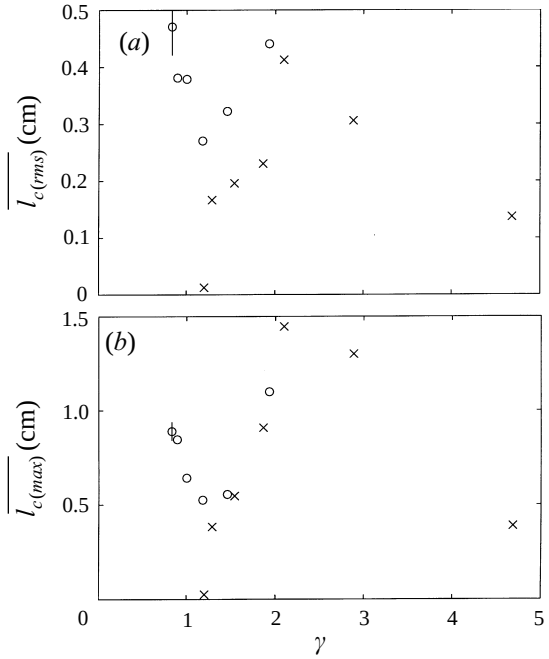


FIGURE 13. The variation of (*a*) cycle-averaged r.m.s. central displacement scale and (*b*) cycle-averaged maximum central displacement scale, with γ: $\times$, $a = 3.1$ cm; $N = 0.615$ rad s^{-1}, $\omega = 0.485$ rad s^{-1}; $\bigcirc$, $a = 3.1$ cm, $N = 0.615$ rad s^{-1}, $\omega = 0.298$ rad s^{-1}.

The temporal variation of the maximum displacement scale $l_{d(max)}$ and the available potential energy of the fluctuations (APEF), defined by

$$\text{APEF} = \frac{g}{\rho_r}\int(\rho(z)-\rho_0(z))\,\mathrm{d}z, \tag{4}$$

over a wave period for the profiles shown in figures 5 and 6 are shown in figure 12. APEF signifies the increase in the potential energy from the monotonized density profile $\rho_0(z)$, which has the minimum potential energy, to that of the measured profile $\rho(z)$ with overturns present. Both quantities showed a strong variation in time within a wave period where consecutive data points in figure 12 are separated in time by 1/7th of the wave period. For each profile, $l_{c(rms)}$ is defined by taking the square root of the averaged sum of squares of all l_c over the boundary layer thickness, and $l_{c(max)}$ is defined as the maximum value of l_c.

Despite the temporal variability, cycle-averaged quantities (denoted by an overbar here) can show the overall features in a given situation. Figure 13 shows the variation of cycle-averaged $\overline{l_{c(rms)}}$ and cycle-averaged $\overline{l_{c(max)}}$ for two series of runs each having the same incident wave amplitude but with varying bed slopes. The incident wave field corresponding to the data points is shown with open circles and have a lower frequency than those marked with $\times$. However, the decrease in averaged lengthscales with increasing γ in figure 13(*a*) is due to the fact that the data were averaged over a smaller boundary layer thickness. It is also interesting to observe that, as the waves become subcritical, the magnitudes of the lengthscales remain comparable to their supercritical counterparts and a maximum near $\gamma \approx 2$ is evident. Owing to experimental limitations, the range of subcritical frequencies covered was limited, although an increase in lengthscales as γ decreased from one can be seen. As can be seen from the linear

https://doi.org/10.1017/S0022112097006939 Published online by Cambridge University Press

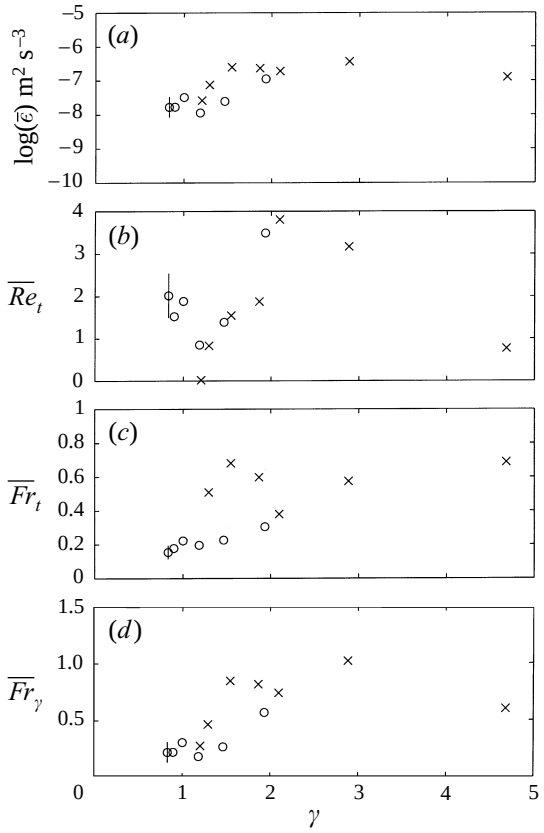


FIGURE 14. The variation of (*a*) cycle-averaged kinetic energy disssipation level, (*b*) cycle-averaged turbulent Reynolds number, (*c*) cycle-averaged turbulent Froude number, (*d*) cycle-averaged small-scale turbulent Froude number, with γ: ×, $a = 3.1$ cm; $N = 0.615$ rad s^{-1}, $\omega = 0.485$ rad s^{-1}; ○, $a = 3.1$ cm; $N = 0.615$ rad s^{-1}, $\omega = 0.298$ rad s^{-1}.

geometric ray considerations, as $\gamma \to 1$ the interaction region between the incident and reflected waves vanishes, and most of the dissipation appears to occur in the above-mentioned narrow flow regime (see the velocity image shown in figure 8, for example). Practical difficulties associated in traversing the probe very close to the slope may also have contributed to the decrease of the lengthscales near $\gamma = 1$.

Figure 14 shows the cycle-averaged kinetic energy dissipation rate $\overline{\epsilon}$, the turbulent Reynolds number $\overline{Re_t}$, the turbulent Froude number $\overline{Fr_t}$, and the small-scale turbulent Froude number $\overline{Fr_\gamma}$ for the same two series described above. The decrease in dissipation levels in the subcritical regime (open circles) is due to the lower incident frequency. Near critical conditions, $\overline{Re_t}$ attains relatively low values due to the decrease in lengthscales. The decrease in the lengthscales and the amount of mixing seems to be in contradiction to the previous experimental studies (Ivey & Nokes 1989) and field measurements (Eriksen 1982) and also to the linear theory. The Reynolds numbers associated with the experiments of Ivey & Nokes (1989) were, however, large compared to those of the present study. The present experiments clearly show that the near-critical wave breaking process is dominated by a highly sheared parallel flow regime just above the bed where most of the incident energy is dissipated. The decrease in turbulent Reynolds numbers suggests that turbulence is suppressed by the viscous forces. The single anomalous points, $\overline{Re_t}$ in figure (14*b*) and high $\overline{Fr_t}$ in figure (14*c*), are

https://doi.org/10.1017/S0022112097006939 Published online by Cambridge University Press

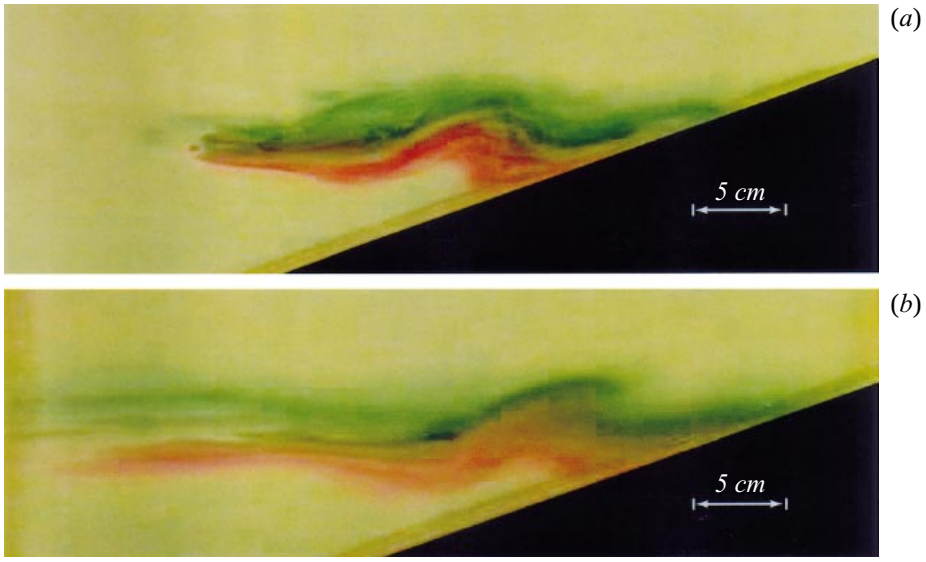


FIGURE 15. Dye visualization of the intrusion flow. The experimental conditions are: $a^* = 2.0$ cm, $N = 0.821$ rad s^{-1}, $\alpha = 45°$, $\beta = 20°$, $\gamma = 2.07$. (*a*) $t = 55T$, (*b*) $t = 125T$. The influence of the wave field on the intrusion is evident near the bed.

due to the low $\overline{l_{c(rms)}}$ recorded in one experiment closer to critical conditions. It should be noted, however, that low $\overline{Fr_\gamma}$ does not necessarily mean that there is no buoyancy flux at some point in the cycle in the wave breaking process; these values are cycle-averaged and in a wave period there could be higher Fr_γ such that during a portion of the wave period $Fr_\gamma > 4$ (there is strong variability in the turbulent properties within a cycle; see figure 12 of Taylor 1993).

3.7. *Formation of intrusions*

In the present study wave breaking occurs at a localized region on the slope, rather different to previous experiments by Taylor (1993) and Ivey & Nokes (1989). Owing to the horizontal pressure gradient between the locally mixed region and the ambient stratification, the mixed fluid intrudes horizontally into the fluid interior along isopycnals. Figure 15 shows dye visualization of the intrusion formation for a supercritically incident wave at two different times. In this particular run, green and red samples of dye, matched at the corresponding densities, were injected slowly at two initial locations approximately 5 cm upslope and 5 cm downslope of the centre of the incident wave ray before starting the paddle.

The upslope and downslope motion parallel to the bed, as described in §3.2, mixed the red and green dye, but only weakly: the mixed fluid then moved horizontally into the main water body. It is worthwhile to note that the colour difference in the dye was maintained for a long time with little mixing between the two dye samples taking place. Figure 16 shows the velocity images obtained over a wave cycle in the intrusion region for the same experiment. At the top in the centre of all panels part of the incident wave can be seen and indeed the dominant motion of the fluid in the figure is wave-like. The horizontal level where the centre of the incident wave rays intersected the bed is shown with a solid line on the left edge of each panel. In the middle of figure (16*a*, *d*) velocity vectors showing fluid motion towards the main water body can be seen, while during the next half of the cycle (figure 16*b*, *c*) the fluid motion in the intrusion region

https://doi.org/10.1017/S0022112097006939 Published online by Cambridge University Press

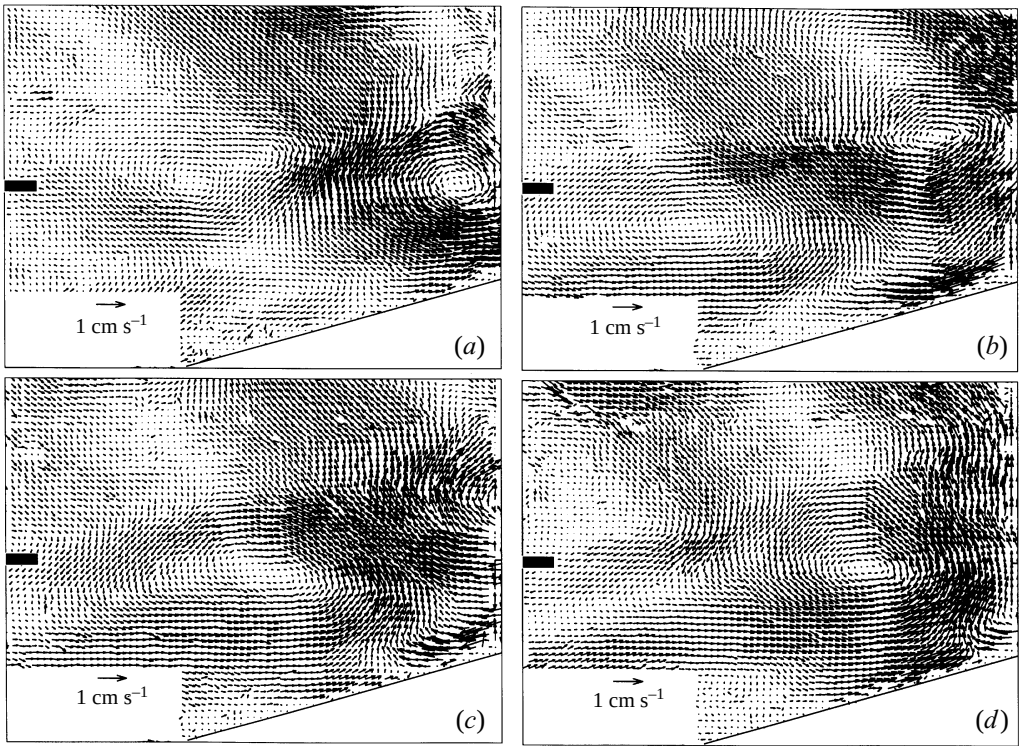


FIGURE 16. The velocity images of the interaction region. The experimental conditions are given in the caption of figure 15. The imaged area shown in each panel is 15.2 cm × 12.2 cm. The horizontal solid line on the left edge of each panel shows the level of the point where the centre of the incident wave ray intersects the bed. The wave period is 10.8 s. (*a*) $t = 60$ s, (*b*) 64 s, (*c*) 66 s, (*d*) 68 s.

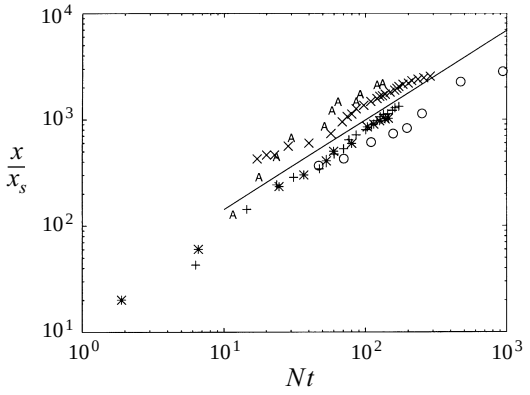


FIGURE 17. The variation of non-dimensional intrusion length with non-dimensional time. ○, $a^* = 2.0$ cm, $N = 0.821$ rad s^{-1}, $\alpha = 45°$, $\beta = 20°$, $\gamma = 2.06$; ×, $a = 3.1$ cm, $N = 0.60$ rad s^{-1}, $\alpha = 52°$, $\beta = 23.3°$, $\gamma = 1.99$; +, $a = 3.1$ cm, $N = 0.60$ rad s^{-1}, $\alpha = 52°$, $\beta = 32.5°$, $\gamma = 1.46$; A, $a = 3.1$ cm, $N = 0.60$ rad s^{-1}, $\alpha = 52°$, $\beta = 16.7°$, $\gamma = 2.74$; ∗, $a = 3.1$ cm, $N = 0.60$ rad s^{-1}, $\alpha = 52°$, $\beta = 36°$, $\gamma = 1.34$.

is in the opposite direction. Thus the intrusion is pulsating, but the result is a net movement driven by the buoyancy flux in the benthic boundary layer of the fluid into the interior.

Depending on an appropriately defined intrusion Richardson number and Reynolds

https://doi.org/10.1017/S0022112097006939 Published online by Cambridge University Press

numbers, the intrusion may have an inertia–buoyancy balance (De Silva & Fernando 1997; Maxworthy & Monismith 1988; Manins 1976; Imberger, Thompson & Fandry 1976), a viscous–buoyancy balance (Maxworthy 1972) or a diffusion–buoyancy balance (Zuluaga-Angel, Darden & Fischer 1972). The parameters in the present study are such that the intrusion lies in the viscous–buoyancy regime (see below); thus, once the intrusion has emerged from the vicinity of the interaction region, a simple viscous–buoyancy balance can be used to obtain the position of the nose and the intrusion velocity.

The volume flux driving the intrusion is due to the turbulent mixing in the interaction region. The flux of incident internal wave energy at the interaction region per unit time is of order $a^2N^2\omega$. If the wave reflection coefficient is C_r, then the energy available for mixing is $a^2N^2\omega(1-C_r)$. Assuming a constant mixing efficiency of R_f (Ivey & Imberger 1991) for the turbulence, the resulting buoyancy flux is $a^2N^2\omega(1-C_r)\,R_f$. Thus we may write,

$$a^2N^2\omega(1-C_r)\,R_f = \frac{g}{\rho_0}\overline{\rho' w'}. \tag{5}$$

The volume flow rate Q per unit width available through turbulent entrainment over an active length of l_a (per unit width) is

$$Q = \frac{l_a}{\rho_0}\overline{\rho' w'}, \tag{6}$$

where ρ' and w' are the density and vertical velocity fluctuations and ρ_0 may conveniently be taken as the mixed density at the depth of the mid-point of the interaction region. Using (5) and (6), and letting $l_a \approx \lambda$, the horizontal wavelength, we get

$$Q = a^2N^2\omega(1-C_r)\,R_f\lambda/g. \tag{7}$$

In general, both R_f and C_r are dependent on the parameter γ. The laboratory experiments of Ivey & Nokes (1990) indicated that R_f is indeed a function of γ and has a maximum near $\gamma \approx 1.2$. The only available information of the functional dependence of C_r on γ is due to the numerical work of Javam *et al.* (1997*b*) who found the best fit of the form

$$C_r = -0.122\gamma^2 + 0.855\gamma - 0.613, \tag{8}$$

a relation which is valid before the initiation of turbulence. The intrusion length–time variation for a buoyancy–viscous intrusion in a linearly stratified is given by (Chen 1980),

$$x \sim (Q^4N^2/\nu)^{1/6}\,t^{5/6}. \tag{9}$$

Using (7)–(9), and noting that $\omega = N\sin\alpha$, the non-dimensional form of the time evolution of intrusion length becomes

$$x/x_s \sim (Nt)^{5/6}, \tag{10}$$

where the normalizing scale x_s is given by

$$x_s = \left[\frac{a^2\lambda}{g}R_f(1-C_r)\sin\alpha\right]^{2/3}(N^9/\nu)^{1/6}. \tag{11}$$

Figure 17 depicts the relationship (9) for different runs. Here we assume $R_f = 0.2$ (e.g. Ivey and Imberger 1991) since γ in the present experiments did not fall within the parameter range of Ivey and Nokes (1990). The solid line indicates the best fit which has a slope of 0.83, in good agreement with the prediction in (10).

https://doi.org/10.1017/S0022112097006939 Published online by Cambridge University Press

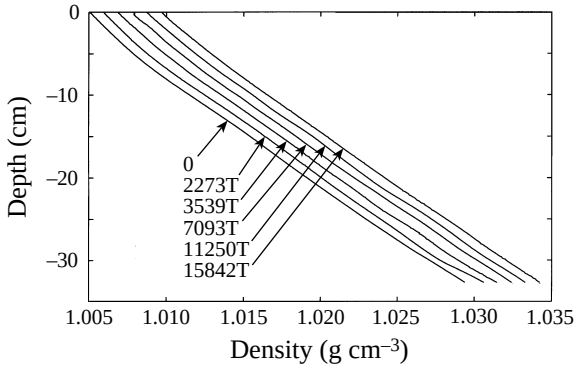


FIGURE 18. The time evolution of the mean density profile, taken 11 cm from the centre of the interaction region to the interior. The experimental conditions are: $a^* = 2.0$ cm, $N = 0.922$ rad s^{-1}, $\alpha = 41.1°$, $\beta = 20°$, $\gamma = 1.92$.

It was assumed above that the intrusion followed a viscous–buoyancy balance. Using typical values of $a = 3$ cm, $\omega = 0.5$ rad s^{-1}, $\lambda = 20$ cm and $\beta = 20°$, we find $Q \sim 3 \times 10^{-3}$ cm^2 s^{-1}. The dynamics of an intrusion (Chen 1980) is determined by the discharge Richardson number $Ri_j = Nh_j/u_j$, the discharge Reynolds number $Re_j = Q/\nu$, and the plume Reynold number $Re_v = (NQ)^{1/2} h_j/\nu$ where h_j is the height of the discharging slot. Based on typical values and taking $h_j = 10$ cm, we find that $Re_v = 42$, $Re_j = 0.3$ and $Ri_j = 120$, which indeed correspond to a viscous–buoyancy balance intrusion (Chen 1980).

Despite the breaking events at the bed, the changes in the mean density gradient were negligibly small. This is shown in figure 18, which shows the vertical density profiles measured in the centre of the tank 11 cm towards the interior from the mid-point of the interaction region. This experiment was run with the intention of looking at the long-term evolution of the mean density gradient in the water column. The wave forcing was sustained over more than 10^4 wave periods, but negligibly small changes in the mean gradients were found. This is somewhat expected because, as pointed out above, the volume flux rate into the fluid interior was small and for this particular run we used the lowest wave amplitude of $a = 2.0$ cm and a somewhat higher stratification than other runs.

We may estimate the rate of destruction of the mean density gradient due to turbulent mixing as follows: the potential energy associated with a linearly stratified fluid column of height H per unit cross-sectional area in the horizontal is $\rho_m N^2 H^3/12$, where ρ_m is the mean density. From above, the buoyancy flux available in the interaction region due to the incident wave energy per unit per volume per unit time is $\rho_m a^2 N^2 \omega$. Thus, equating the buoyancy flux to the rate of change of the potential energy, and taking the height of the mixed region H as the thickness of the benthic boundary layer δ, we may write

$$\frac{\mathrm{d}}{\mathrm{d}t}(\rho_m N^2 \delta^3) \sim \rho_m a^2 N^2 \omega \delta R_f (1 - C_r). \tag{12}$$

The averaged thickness of the boundary layer δ remains constant over a time scale long compared to the wave period. Non-dimensionalizing the time by $1/\omega$ ($\tau \sim \omega t$), the time rate of change of stratification at large times, becomes

$$\left| \frac{1}{N^2} \frac{\mathrm{d}}{\mathrm{d}\tau}(N^2) \right| \sim \left(\frac{a}{\delta} \right)^2 R_f (1 - C_r). \tag{13}$$

https://doi.org/10.1017/S0022112097006939 Published online by Cambridge University Press

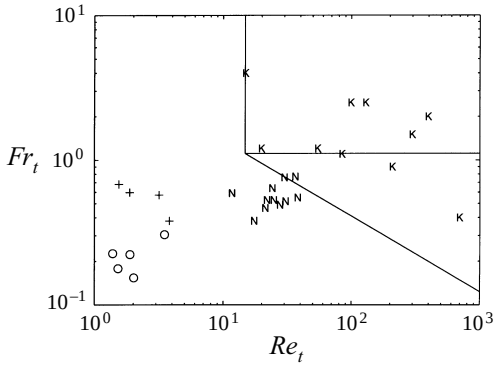


FIGURE 19. The data points in the Fr_t, Re_t diagram: +, ○, present study; *N*, laboratory experiments of Grigg & Ivey (1997) on mixing due to shear instabilities; K, field measurements of Lemckert & Imberger (1995).

In general $a/\delta < 1$ for supercritical waves, as shown in figure 7. While R_f and C_r are not known accurately, reasonable estimates would be $R_f < 0.2$, and $1 - C_r < 1$. Therefore, we expect $|(\mathrm{d}N^2/\mathrm{d}\tau)/N^2| \ll 1$. Hence the destruction of the mean density gradient is rather slow. A basic assumption in deriving equation (13) is that the energy input to the boundary mixing region remains constant. However, as the stratification within this region (and also near the paddle) decreases, the energy input in the form of internal waves diminishes; hence (13) does not predict the behaviour at large times.

3.8. *Comparison with field observations*

The internal wave field in lakes and oceans consists of a broad band of frequencies and wavenumbers. Lack of detailed knowledge of the incident and reflected wave fields in field observations makes it fundamentally difficult to compare such results with the present experimental study. The dependence of a stratifying agent, heat in freshwater lakes, and heat and salt in the oceans, on the turbulent quantities and the vertical fluxes is also not known.

Figure 19 shows the experimental data in Fr_t, Re_t space (see Ivey & Imberger 1991). Also included in the figure are some field measurements of boundary mixing. Measurements by Lemckert & Imberger (1995) in Lake Kinneret clearly show a buoyancy flux. Diffusivities of the order of $10^{-4}\,\mathrm{m^2\,s^{-1}}$ with $Fr_\gamma = 24$ have been reported by Toole *et al*. (1994). Ledwell & Hickey (1995) estimated diffusivities as high as $3 \times 10^{-4}\,\mathrm{m^2\,s^{-1}}$ and non-dimensional dissipation rates as high as $Fr_\gamma = 19$ in the Santa Monica basin due to boundary mixing. However, measurements by Van Haren *et al*. (1994) did not indicate any buoyancy flux, in spite of very high dissipations rates and values of $Fr_\gamma = 20$. The present data, characterized by relatively low Re_t, fall in a viscous-dominated regime. According to Ivey & Imberger (1991) this should not provide any buoyancy flux.

The potential energy associated with an overturn of the scale of l_c is $l_c^2 N^2$ which may be taken as a scale for the APEF (§3.6). A simple manipulation yields

$$\frac{\epsilon}{N(\mathrm{APEF})} \sim Fr_t^3. \tag{14}$$

Since the Froude numbers encountered in the experiment are in general less than unity, (14) implies that $\epsilon/N \ll$ APEF. This shows how strong the buoyancy forces are, so that

https://doi.org/10.1017/S0022112097006939 Published online by Cambridge University Press

the potential energy associated with the overturns is much higher than the dissipation of turbulent kinetic energy during a buoyancy (or wave) period.

4. Conclusions

An experimental study on the turbulence generated by an internal wave ray breaking on a sloping bed was presented over a parameter range which covered subcritical, critical and supercritical frequencies ($0.83 < \gamma < 4.5$). The present configuration differed from previous laboratory (Ivey & Nokes 1989, 1990; Taylor 1993) and possibly field studies (Eriksen 1982, 1985; Lemckert & Imberger 1995) in that the incident wave ray covered only a fraction of the length of the bottom slope.

Flow visualization revealed that as the incident waves became progressively supercritical the instabilities were first initiated away from the bed. Flow visualization and velocity measurements showed that near critical conditions the flow was confined to a narrow region above the bed. In this case, most of the incident wave energy was dissipated in a thin region. Thus, small values of the turbulent lengthscale l_c and hence low turbulent Reynolds numbers were observed. For the cases of subcritical and supercritical incident waves, internal wave reflection from the sloping bed could be thought of as wave–wave interaction between the incident and the reflected waves. As given by (3), the area of the interaction region increases progressively as the waves depart from critical conditions. The central displacement lengthscale and the turbulent Reynolds number increased steadily up to about $\gamma \approx 2$, after which they both started to decrease.

The mixed fluid generated at the boundary communicated with the main water body in the form of a horizontal intrusion which propagated along the isopycnal surface that intersected the centre of the interaction region. In the present study, the Reynolds number of the turbulence due to wave breaking was low. This was also reflected in the spreading of the intrusion which followed a two-dimensional viscous–buoyancy balance.

The efficiency of mixing in converting incident wave energy into potential energy by the breaking of internal waves at the slope is still debatable. Efficiencies as high as 0.2 have been reported in laboratory experiments by Ivey & Nokes (1989); Taylor (1993) reported slightly lower values; certain field studies showed higher conversion efficiencies (Lemckert & Imberger 1995) while some did not identify any fluxes (Van Haren *et al.* 1994). Data points from the present study shown in Fr_t, Re_t space (figure 19) indicate that no buoyancy flux should occur in the parameter range considered. However, there is enough buoyancy flux taking place in the wave interaction region to sustain a weak buoyancy–viscous intrusion. The conversion is insignificant in that no measurable change in the mean density gradient was observed (figure 18). On the other hand, in lakes the benthic fluid carries abundant nutrients, hence such intrusions distribute the nutrients essential for plant and animal life. Thus, from a biological point of view in terms of transporting nutrient-rich benthic water into the interior, the mixing along the slope driven by the wave breaking is an important means of exchange between boundary layer and the interior.

The present experiments considered only the case where the incoming waves were monochromatic and two-dimensional before the initiation of instabilities. To understand the problem fully, the three-dimensional nature of the flow field has to be examined. However, the complexities that exist in natural water bodies, compared to the simplified laboratory and theoretical models, add immense difficulties to the understanding of the important role played by the turbulent benthic boundary layer.

https://doi.org/10.1017/S0022112097006939 Published online by Cambridge University Press

Therefore, it is natural to extend the analysis of wave breaking to more realistic situations encountered in nature. The beds found in the natural environment are non-uniform, rough, and far from being planar. Gilbert & Garrett (1989) considered the case of wave breaking on irregular bottom slopes and concluded that the energy enhancement and associated dissipation rates are higher on a convex topography than on a concave topography. Experiments on wave breaking on hydraulically rough beds, or beds of soft sediments, have not yet been looked at. The interaction of a very thin sediment layer at the bed and a relatively thick benthic boundary layer in the context of transport of nutrients remains to be examined.

The authors wish to thank Seng Giap Teoh and John Devitt for their help in conducting the experiments. Comments by the participants of the IUTAM conference in Broome are gratefully acknowledged. I. P. De S. would like to thank Professor Joe Fernando for his continued encouragement. The authors would also like to acknowledge the careful and constructive criticisms of the anonymous referees in strengthening the paper. This project was supported by the Centre for Environmental Fluid Dynamics and the Australian Research Council. This paper forms Centre for Water Research reference ED-1069-PDS.

REFERENCES

Armi, L. 1978 Some evidence for boundary mixing in the deep ocean. *J. Geophys. Res.* **83**, 1971–1979.

Baccini, P. 1985 *Chemical Processes in Lakes* (ed. W. Stumm). John Wiley & Sons.

Batchelor, G. K. 1959 Small-scale variation of convected quantities like temperature in a turbulent fluid. Part 1: General discussion and the case of small conductivity. *J. Fluid Mech.* **5**, 113–133.

Bell, T. H. 1975 Statistical features of sea-floor topography. *Deep-Sea Res.* **22**, 883–892.

Cacchione, D. & Wunsch, C. 1974 Experimental study of internal waves over a slope. *J. Fluid Mech.* **66**, 223–239.

Chen, J.-C. 1980 Studies on gravitational spreading currents. PhD Dissertation, California Institute of Technology.

De Silva, I. P. D. & Fernando, H. J. S. 1997 The collapse of a turbulent mixed region in a stratified fluid. *J. Fluid Mech.* (submitted).

De Silva, I. P. D., Imberger, J. & Ivey, G. N. 1995 Internal wave energised benthic boundary layer transport. *IUTAM Symp. on Physical Limnology*, *Broome*, *Western Australia*, pp. 399–407.

Dillon, T. M. & Caldwell, D. R. 1980 The Batchelor spectrum and dissipation in the upper ocean. *J. Geophys. Res.* **85**, 1910–1916.

Eriksen, C. C. 1982 Observations of internal wave reflection off sloping bottoms. *J. Geophys. Res.* **87**, 525–538.

Eriksen, C. C. 1985 Implications of ocean bottom reflection for internal wave spectra and mixing. *J. Phys. Oceanogr.* **15**, 1145–1156.

Etemad-Shahidi, A. & Imberger, J. 1997 Anatomy of turbulence in thermally stratified lakes. *J. Phys. Oceanogr.* (submitted).

Garrett, C. 1979 Comments on "some evidence for boundary mixing in the deep ocean", by L. Armi. *J. Geophys. Res.* **84**, 5095.

Garrett, C., MacCready, P. & Rhines, P. 1993 Boundary mixing and arrested Ekman layers: Rotating stratified flow near a sloping boundary. *Ann. Rev. Fluid Mech.* **25**, 291–323.

Gilbert, D. & Garrett, C. 1989 Implications for ocean mixing of internal wave scattering off irregular topography. *J. Phys. Oceanogr.* **19**, 1716–1729.

Grigg, N. & Ivey, G. N. 1997 A laboratory investigation into shear-generated mixing in a salt wedge estuary. *Geophys. Astrophys. Fluid Dyn.* **85**, 65–95.

Howes, W. L. 1984 Rainbow Schlieren and its applications. *Appl. Opt.* **23**, 2449–2460.

https://doi.org/10.1017/S0022112097006939 Published online by Cambridge University Press

Howes, W. L. 1985 Rainbow Schlieren vs Mach-Zender interferometer: a comparison. *Appl. Opt.* **24**, 816–822.

Imberger, J. 1994 Transport processes in lakes: A review. In *Limnology Now: A Paradigm of Planetary Problems* (ed. R. Margalef), pp. 99–193. Elsevier.

Imberger, J. 1995 Flux path in a stratified lake: A Review. *IUTAM Symp. on Physical Limnology, Broome, Western Australia*, pp. 423–439.

Imberger, J. & Boashash, B. 1986 Application of the Wigner–Ville distribution to temperature gradient microstructure: A new technique to study small-scale turbulence. *J. Phys. Oceanogr.* **16**, 1997–2012.

Imberger, J. & Ivey, G. N. 1993 Boundary mixing in stratified reservoirs. *J. Fluid Mech.* **248**, 477–491.

Imberger, J., Thompson, R. & Fandry, C. 1976 Selective withdrawal from a finite rectangular tank. *J. Fluid Mech.* **78**, 489–512.

Itsweire, E. C., Helland, K. N. & Van Atta, C. W. 1986 The evolution of grid generated turbulence in a stably stratified fluid. *J. Fluid Mech.* **162**, 299–338.

Ivey, G. N., De Silva, I. P. D. & Imberger, J. 1995 Internal waves, bottom slopes and boundary mixing. *Aha Hulikoa, Hawaiian Winter Workshop on Topographic Effects in the Ocean, Honolulu, Hawaii*, pp. 199–205.

Ivey, G. N. & Imberger, J. 1991 On the nature of turbulence in a stratified fluid. Part I: The energetics of mixing. *J. Phys. Oceanogr.* **21**, 650–658.

Ivey, G. N. & Nokes, R. I. 1989 Vertical mixing due to the breaking of critical internal waves on sloping boundaries. *J. Fluid Mech.* **204**, 479–500.

Ivey, G. N. & Nokes, R. I. 1990 Mixing driven by the breaking of internal waves against sloping boundaries. *Proc. Intl Conf. on Physical Modelling of Transport and Dispersion, MIT, Boston*, pp. 11A3–11A8.

Javam, A., Imberger, J. & Armfield, S. 1997*a* Numerical study of internal wave–wave interactions. *J. Fluid Mech.* (submitted).

Javam, A., Imberger, J. & Armfield, S. 1997*b* Numerical study of internal wave overturning on a sloping boundary. *J. Fluid Mech.* (submitted).

Ledwell, J. R. & Hickey, B. M. 1995 Evidence for enhanced boundary mixing in the Santa Monica basin. *J. Geophys. Res.* **100**, 20665–20679.

Lemckert, C. & Imberger, J. 1995 Turbulent boundary layers in fresh water lakes. *IUTAM Symp. on Physical Limnology, Broome, Western Australia*, pp. 409–422.

Luketina, D. A. 1987 Frontogenesis of freshwater overflow. PhD dissertation, University of Western Australia.

Luketina, D. A. & Imberger, J. 1989 Turbulence and entrainment in a buoyant surface plume. *J. Geophys. Res.* **94**, 12619–12636.

Manins, P. C. 1976 Intrusion into a stratified fluid. *J. Fluid Mech.* **74**, 547–560.

Maxworthy, T. 1972 Experimental and theoretical studies of horizontal jets in a stratified fluid. *Intl Symp. on Stratified flow, Novosibirsk*, pp. 611–618.

Maxworthy, T. & Monismith, S. G. 1988 Differential mixing in a stratified fluid. *J. Fluid Mech.* **189**, 571–598.

McEwan, A. D. 1973 Interactions between internal gravity waves and their traumatic effect on a continuous stratification. *Boundary-Layer Met.* **5**, 159–175.

McEwan, A. D. 1983 The kinematics of stratified mixing through internal wave breaking. *J. Fluid Mech.* **128**, 47–57.

Munk, W. H. 1966 Abyssal recipes. *Deep-Sea Res.* **13**, 207–230.

Ogihara, Y. 1997 Propagation of internal waves through a stratified lake. PhD Dissertation, University of Western Australia.

Phillips, O. M. 1977 *The Dynamics of the Upper Ocean*. Cambridge University Press.

Slinn, D. N. & Riley, J. J. 1996 Turbulent mixing in the oceanic boundary layer due to internal wave reflection from sloping terrain. *Dyn. Atmos. Oceans* **23**, 51–62.

Stevens, C. L. & Coates, M. J. 1994 An automated velocity field measurement technique for laboratory experiments. *Intl J. Hydr. Res.* **32**, 195–212.

https://doi.org/10.1017/S0022112097006939 Published online by Cambridge University Press

Stillinger, D. C., Helland, K. N. & Van Atta, C. W. 1983 The evolution of grid-generated turbulence in a stably stratified fluid. *J. Fluid Mech.* **162**, 299–338.

Taylor, J. R. 1993 Turbulence and mixing in the boundary layer generated by shoaling internal waves. *Dyn. Atmos. Oceans* **19**, 233–258.

Teoh, S. G., Ivey, G. N. & Imberger, J. 1997 Laboratory study of the interactions between two internal wave rays. *J. Fluid Mech.* **336**, 91–122.

Thorpe, S. A. 1977 Turbulence and mixing in a Scottish Loch. *Phil. Trans. Proc. R. Soc. Lond.* A **286**, 125–181.

Thorpe, S. A. 1987 On the reflection of a train of finite-amplitude internal waves from a uniform slope. *J. Fluid Mech.* **178**, 279–302.

Thorpe, S. A. & Haines, A. P. 1987 Appendix to On the reflection of a train of finite-amplitude internal waves from a uniform slope. *J. Fluid Mech.* **178**, 299–302.

Thorpe, S. A., Hall, P. & White, M. 1990 The variability of mixing on a continental slope. *Proc. R. Soc. Lond.* A **439**, 115–130.

Toole, J. M., Polzin, K. L. & Schmitt, R. W. 1994 Estimates of diapycnal mixing in the abyssal ocean. *Science* **264**, 1120–1123.

Van Haren, H., Oakey, N. & Garrett, C. 1994 Measurements of internal wave band eddy fluxes above a sloping bottom. *J. Mar. Res.* **52**, 909–946.

White, M. 1994 Tidal and subtidal variability in the sloping benthic boundary layer. *J. Geophys. Res.* **99**, 7851–7864.

Wolanski, E. 1987 Some evidence for boundary mixing near coral reefs. *Limnol. Oceanogr.* **32**, 735–739.

Wu, J. 1969 Mixed region collapse with internal wave generation in a density-stratified medium. *J. Fluid Mech.* **35**, 531–544.

Wuest, A., Van Senden, D. C., Imberger, J., Piepke, G. & Gloor, M. 1994 Diapycnal diffusivity measured by microstructure and tracer techniques – A comparison. *Intl Symp. on Stratified Flows*, *Grenoble*, *France*, Vol. **3**, pp. B5–8.

Wunsch, C. & Hendry, R. 1972 Array measurements of the bottom boundary layer and the internal wave field on the continental slope. *Geophys. Fluid Dyn.* **4**, 101–145.

Zuluaga-Angel, A. A., Darden, R. B. & Fischer, H. B. 1972 Fluid into a stratified reservoir. *Rep.* EPA-R2-72-037. US Environmental Protection Agency, Washington, DC.

https://doi.org/10.1017/S0022112097006939 Published online by Cambridge University Press